Experimental Validation of Attitude and Rate Sensor Bias Filter using Range-difference Measurements*

Erlend K. Jørgensen[1], Thor I. Fossen[2], Ingrid Schjølberg[1], Paulo T. T. Esperança[3]

[1]Department of Marine Technology
Norwegian University of Science and Technology (NTNU)
Trondheim, Norway

[2]Department of Engineering Cybernetics
Norwegian University of Science and Technology (NTNU)
Trondheim, Norway

[3]Department of Naval Engineering
Federal University of Rio de Janeiro (UFRJ)
Rio de Janeiro, Brazil

***Abstract*—This paper considers the problem of constructing a filter for estimating attitude and rate sensor bias, that has both proven stability and close-to-optimal performance with respect to noise. The filter is based on measuring the difference in time of arrival for signals sent from three or more known, fixed positions to two or more receivers on the vehicle. An inertial measurement unit is also used, both rate sensor and accelerometer measurements, and a position estimate is needed, generated from depth and time of arrival measurements. The vectors between receivers on the vehicle are assumed to be known in the body frame, and are calculated in the inertial frame through an algebraic transformation. These vectors are used as input for a non-linear observer along with rate sensor and accelerometer data, estimating Euler angles and rate sensor bias. These estimates are used as a linearization point for a Linearized Kalman Filter, taking the full non-linear system into account. Two experiments are run, and the filter is compared to an Extended Kalman Filter, and a non-implementable Linearized Kalman Filter using the true state as linearization point.**

***Keywords*—attitude estimation; non-linear filtering; exogenous kalman filter; linearized kalman filter**

I. INTRODUCTION

Robust and accurate position and attitude estimation is an important part in reaching the goal of autonomy for underwater vehicles. A common approach for positioning is to use an underwater long base-line (LBL) network, measuring the time of arrival (TOA) of acoustic signals from several fixed, known positions. These measurements relate directly to the range, and from these ranges position can be calculated. This paper builds on the work presented in Jørgensen and Schjølberg[20], where the LBL network is used to determine the yaw angle of the vehicle. This is done by placing several receivers on the vehicle, and measuring the difference in TOA between the receivers. If the LBL system is already in place, this means adding one or more extra receivers on the vehicle, yielding only a small increase in infrastructure. Similar approaches can be found for surface vehicles, in which several GPS antennas are placed on the vehicle, and the measurements are used to determine attitude[27][6].

It is possible to measure angular velocities with rate sensors, usually a part of an inertial measurement unit (IMU), but these measurements are often corrupted by biases and noise. Consequently, simply integrating the rate sensor output will not give accurate attitude estimates, and some extra measurements relating directly to the attitude is necessary. A common approach is to use two or more non-parallell reference vectors known in either the body- or the global frame, and measured in the other. These can be used to determine attitude[25]. For constant reference vectors, a non-linear observer (NLO) for estimating attitude and rate sensor bias with global stability properties was suggested by Hamel and Mahony[14], and extended to time-varying reference vectors by Grip et al.[11]. Traditionally these methods have been applied using the measured acceleration from the accelerometer combined with either magnetometer- or gyrocompass measurements. Other approaches for non-linear attitude determination are suggested for example in Sabatini[23] and Salcudean[24], and a survey can be found in Crassidis et al.[7].

It is common to use two reference vectors to determine attitude for underwater vehicles: accelerometer measurements combined with either magnetometer- or gyrocompass measurements. These are used as input to the NLO for estimating attitude. The acceleration vector in the global frame is assumed to be the gravity vector, and the magnetic field in the global frame is assumed to be known beforehand. For small accelerations (which is usually the case for underwater vehicles, especially autonomous vehicles), the gravity vector will be dominating, and the acceleration measurement will therefore give good results. However, the second reference vector measurement, provided by either magnetometer or gyrocompass has some drawbacks. The magnetometer is prone to disturbances; the

*This work is supported by the NTNU Center of Autonomous Marine Operations and Systems (NTNU AMOS), grant no. 223254.

magnetic field can be varying over time and position, as well as local disturbances from thrusters and electronics. The gyrocompass is very accurate, but is heavy, large, expensive and requires recalibration. As a result of this, it is suggested and demonstrated in this paper how to use the acoustic LBL system for providing extra reference vector measurements in addition to the acceleration measurement.

By using the difference-in-time-of-arrival (DTOA), it is possible to calculate the reference vectors in the global frame, while it is assumed the reference vectors are known in the body frame. The length of the vectors are naturally dependent on the size of the underwater vehicle, but in general the demand for accurate calibration and DTOA measurements increases with smaller distance between receivers. However, these measurements are assumed to be unbiased, and not distorted over time or with changing vehicle position. A similar approach can be found in Batista et al.[4], in which a NLO is suggested, based on a combination of LBL, Ultra Short BaseLine (USBL) and rate sensor measurements.

The goal of the work is to develop a filter with proven stability and close-to-optimal performance wrt. bounded noise, for determining attitude and rate sensor bias without employing magnetometer or gyrocompass measurements. This can increase robustness and redundancy for underwater vehicle attitude estimation. Filter design, stability analysis and simulations have been carried out in [20], and consequently experimental validation is the next step. The main contribution of this paper is a full experimental validation of the filter suggested in [20]. Furthermore, the filter is compared to an Extended Kalman Filter (EKF) and a non-implementable optimal Linearized Kalman Filter (LKF) to validate the claim that the filter has close-to-optimal stationary performance, and similar stationary performance as the EKF. The experiments were performed in LabOceano, a lab testing facility at the Federal University of Rio de Janeiro. The filter is also modified slightly from [20] to relax one of the assumptions stated, in which one of the receivers has to be in the origin of the body frame. Furthermore, implementation aspects and practical issues are discussed and solutions to these issues are proposed.

A. The eXogenous Kalman Filter

The presented filter is based on the eXogenous Kalman Filter (XKF) principle, in which an exogenous state estimate provided by a globally stable auxiliary estimator is used as a linearization point for a LKF. As is shown in Johansen and Fossen[17], under certain assumptions and if the system has certain properties, this results in a filter with proven stability and with close-to-optimal noise properties. The globally stable auxiliary estimator has proven stability properties, but does not have close-to-optimal noise properties. This is in contrast to the EKF, which has close-to-optimal noise properties, but no proven stability for the given model, resulting in potentially unpredictable and unstable behaviour. The computational complexity of the XKF is larger than the EKF, as an auxiliary estimator needs to be run in addition to the LKF. However, the computational load is small compared to other, more robust alternatives to the EKF such as the particle filter or Monte-Carlo filter. For more examples of the XKF, see [16][19].

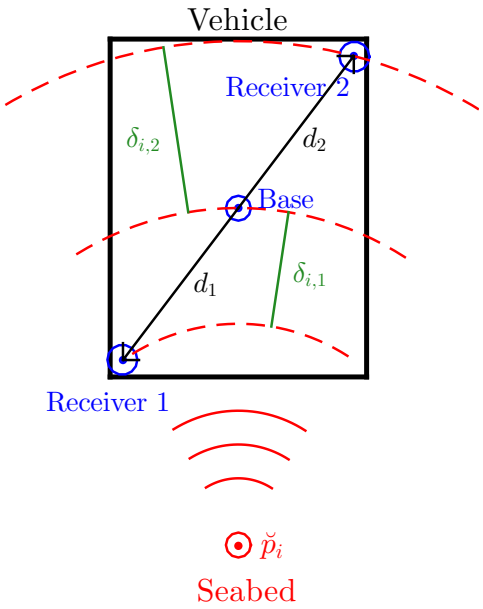

Fig. 1: Illustration of system with range difference measurements. Variables are defined and explained in Sec. II-C.[20]

The paper is organized as follows. Section II describes how to transform the original measurements into the computed measurements. Section III shows the overall structure of the filter, and presents details about each step. Section IV discusses the practical aspects, regarding system setup, calibration of equipment and implementation of the filters. Section V provides the results, Section VI gives a short discussion regarding the results and possible improvement of the system, and Section VII holds the conclusion.

II. COMPUTED MEASUREMENTS

A. Acoustic System Description

The acoustic system consists of N senders with fixed, known positions located on the seafloor, and $M+1$ receivers with fixed, known positions located on the vehicle. Acoustic signals are sent simultaneously from each sender, and the TOA is measured from each sender at each receiver. One receiver is chosen as the "base receiver" and the vectors from this receiver to the other receivers in the body frame are denoted $d_{1,\dots,M}$. The DTOA between the base receiver and the other receivers are calculated, converted to ranges, and from these measurements the vectors can be calculated in the global frame, and used to determine attitude. An illustration of the system is shown in Fig. 1.

B. Attitude Representation

In the suggested filter, the attitude is described by Euler angles, $\mathbf{\Theta} = [\phi, \theta, \psi]^T$. This is an intuitive way of representing attitude, and fits well with the acceleration measurement, in which two out of three Euler angles can be determined. A well known drawback of the Euler angles are singularities, resulting in only a locally stable filter. However, these singularities are well defined, and as mentioned in [9], it is possible to change representation if the filter is approaching one of the singularities. Alternatively, unit quaternions can be used [21]. The representation chosen is the same as in [9], the roll-pitch-yaw sequence, in which the singularities will be at $\theta = \pm\frac{\pi}{2}$, as having a pitch angle of $\pm\frac{\pi}{2}$ is a rare state for the type of Remotely Operated Vehicles (ROVs) used in underwater operations today.

C. Measurement Models

The two coordinate frames used in the measurement models are the body frame, and the North-East-Down (NED) frame approximated as a local inertial frame with origin defined by the Qualisys camera positioning system, described in more detail in Sec. IV-A.

The outputs from the IMU applied in the filter are accelerometer measurements and rate sensor measurements. The IMU is fixed on the ROV and thus follows the body frame, known as a strapdown system. Consequently, the measurements of both acceleration, $\mathbf{a}^b_{imu}$, and angular velocity, ω^b_{imu}, is in the body frame. Traditionally these IMU measurements are modeled as

$$\mathbf{a}^b_{imu} = \mathbf{a}^b + \mathbf{R}^b_n \mathbf{g}^n + \mathbf{b}_a + \epsilon_a = \mathbf{R}^b_n(\mathbf{a}^n + \mathbf{g}^n) + \mathbf{b}_a + \epsilon_a \quad (1)$$

$$\omega^b_{imu} = \omega^b_{b/n} + \mathbf{b} + \epsilon_\omega \quad (2)$$

where $\mathbf{a}^i$ is the vehicle acceleration in coordinate frame i, $\mathbf{g}^n$ is the gravity vector in the NED frame, $\mathbf{R}^b_n$ is the rotation matrix from the NED frame to the body frame, $\mathbf{b}_a$ is a slowly time-varying acceleration measurement bias, $\mathbf{b}$ is a slowly time-varying rate sensor bias and ϵ_a and ϵ_ω are zero-mean Gaussian white noise vectors with covariances $\mathbf{Q}_a$ and $\mathbf{Q}_\omega$.

In this paper it is assumed that the accelerometer bias is compensated for in a calibration scheme, either pre-calibration or online estimation of the bias. Examples of pre-calibration schemes can be found in [5][28], and online calibration schemes can be found in [13][8][5]. If the accelerometer bias is calibrated beforehand, the performance of the filter might deteriorate over time, as accelerometer bias is assumed to be slowly time-varying. Consequently, if a pre-calibration scheme is applied the accelerometer bias should be re-calibrated after some time period, depending on the quality of the accelerometer. Furthermore, it is assumed that for ROVs performing underwater operations the acceleration of the vehicle is small enough to be negligible compared to the gravity vector. The resulting acceleration measurement model is a simplified version of (1) given by

$$\mathbf{a}^b_{imu} \approx \mathbf{R}^b_n \mathbf{g}^n + \epsilon_a \quad (3)$$

The model of the range difference measurements is based on the system described in Sec. II-A. The position of the base receiver is defined as $\mathbf{p}^n = [x, y, z]^T$ and the position of sender i is defined as $\breve{\mathbf{p}}^n_i = [\breve{x}_i, \breve{y}_i, \breve{z}_i]^T$, both in the NED frame. The geometric range is defined as $\rho_i = ct_i = ||\mathbf{p}^n - \breve{\mathbf{p}}^n_i||$ where c is the wave speed, t_i is the TOA from sender i and $||\cdot||$ is the 2-norm. In Stovner et al.[26] an acoustic range measurement is given as

$$y_i = \frac{1}{\sqrt{\beta}}(\rho_i + \epsilon_{y,i}) \quad i = 1, .., N \quad (4)$$

where $\epsilon_{y,i}$ is zero-mean Gaussian white noise with variance $\sigma^2_{y,i}$ and β is an unknown, multiplicative parameter to take into account uncertainty in the underwater acoustic wave speed. These are referred to as pseudo-range measurements as they are a function of the geometric range, but also an unknown parameter, β. Based on this formulation, each pseudo-range difference, $\delta_{i,j}$, is modeled as

$$\delta_{i,j} = \frac{1}{\sqrt{\beta}}\left(||\mathbf{p}^n + \mathbf{R}^n_b \mathbf{d}^b_j - \breve{\mathbf{p}}_i{}^n|| - \rho_i + \epsilon_{\delta,i,j}\right), \quad i = 1, .., N,\ j = 1, .., M \quad (5)$$

where $\epsilon_{\delta,i,j}$ is zero-mean Gaussian white noise with variance $\sigma^2_{\delta,i,j}$ and $\mathbf{d}^b_j$ is vector j between receivers, expressed in the body frame. Furthermore, depth measurements are also employed, modeled as

$$z_m = z + \epsilon_z \quad (6)$$

where ϵ_z is assumed to be zero-mean Gaussian white noise with variance σ^2_z.

Assumption 1. *At least one of the vectors between receivers,* $\mathbf{d}^n_j$*, will be non-parallel with* $\mathbf{g}^n$ *for all t, i.e.*[20]

$$\exists\, c \quad s.t. \sum_{j\in\{1,..,M\}} ||\mathbf{g}^n \times \mathbf{d}^n_j|| \geq c > 0 \quad \forall\, t$$

In practice this means that if there is only two receivers on the vehice, resulting in one vector between receivers, $\mathbf{d}^n_1$, then $\mathbf{d}^n_1$ must never be parallell to the gravity vector. If $\mathbf{d}^n_1$ is along the body x-axis, the requirement would mean not having a pitch angle of $\theta = \pm\pi/2$, which are the same angles as the singularities in the filter, and as mentioned above, is not a natural state for most ROVs used in underwater operations today. However, if there are three non-collinear receivers on the vehicle, the system will have two non-parallell vectors between receivers, and Assumption 1 will always be true.

D. Calculate Roll Angle and Pitch Angle

The calculation of vectors between receivers, $\mathbf{d}^n_{1,..,M}$, described in Sec. II-E is significantly more robust if estimates of roll angle and pitch angle are already available. In this case, the TDOA measurements are only used to calculate yaw angle. As described in [9], it is possible to calculate roll angle and pitch angle directly from the accelerometer measurements, given that bias is compensated for, and the vehicle is stationary. It is rarely the case that the vehicle is completely stationary, but as long as the accelerations are small, gravity is the dominating factor and the calculated roll angle and pitch angle will be fairly accurate. As discussed in Sec. II-C, it is assumed that for ROVs performing underwater operations it is assumed that accelerations will be small. This is also discussed in [8], in which a scheme is suggested where roll angle and pitch angle are only calculated when the acceleration is below a certain threshold. It is also possible to account for the acceleration by creating a feedback loop in which the estimated acceleration is subtracted from the acceleration measurements, as described in for example [18], or by having an auxiliary filter estimate this acceleration. As this increases the complexity of the filter, this has not been done in the applied filter, and is considered potential further work. Consequently, the accelerations of the vehicle are assumed to be negligible compared to the gravity vector.

When calculating roll angle and pitch angle, the formulas are modified slightly from the ones given in [9], to make them more robust close to the singularities. Furthermore, the $\mathrm{atan2}$-function is used instead of the $\arctan$-function, to consider also which quadrant the solution is in. The accelerometer output is given as $\mathbf{a}^b_{imu} = [a_x, a_y, a_z]^T$, the formulas for roll angle, ϕ, and pitch angle, θ, are given by

$$\theta \approx \mathrm{atan2}\left(-a_x\ ,\ \sqrt{a_y^2 + a_z^2}\right) \tag{7}$$

$$\phi \approx \mathrm{atan2}\left(\mathrm{s}_1 \cdot a_y\ ,\ s_1 \cdot s_2 \cdot \sqrt{a_z^2 + k_1 \cdot a_x^2}\right) \tag{8}$$

where $s_1 = \mathrm{sign}(\cos(\theta))$, $s_2 = \mathrm{sign}(\mathrm{a_z})$. atan2 is given by

$$\mathrm{atan2}(y,x) = \begin{cases} \arctan\left(\frac{y}{x}\right) & \text{if } x > 0 \\ \arctan\left(\frac{y}{x}\right) + \pi & \text{if } x < 0 \text{ and } y \geq 0 \\ \arctan\left(\frac{y}{x}\right) - \pi & \text{if } x < 0 \text{ and } y < 0 \\ +\frac{\pi}{2} & \text{if } x = 0 \text{ and } y > 0 \\ -\frac{\pi}{2} & \text{if } x = 0 \text{ and } y < 0 \\ \text{undefined} & \text{if } x = 0 \text{ and } y = 0 \end{cases} \tag{9}$$

k_1 is zero except for when θ is close to $\pm\frac{\pi}{2}$, given by

$$k_1 = (A + A \cdot \tanh(B \cdot (|\theta| - 1.43))) \cdot (A - A \cdot \tanh(B \cdot (|\theta| - 1.71))) \tag{10}$$

where $A = \sqrt{0.1}/2$ and $B = 200$. The values of A and B are chosen based on experience from simulations, therefore different values might give better results, depending on the accelerometer used and its noise characteristics.

The calculated values for θ and ϕ will both be used in calculating the vectors $\mathbf{d}^n_{1,..,M}$ as described in the following section, and as measurements of roll angle and pitch angle in the LKF described in Sec. III-D.

E. Calculate Vectors Between Receivers, $\mathbf{d}^n_{1,..,M}$

Based on the pseudo-range difference measurement model in (5) and that for a vector $\mathbf{v}$, $||\mathbf{v}|| = \sqrt{\mathbf{v}^T\mathbf{v}}$, each pseudo-range difference measurement can be written as

$$\delta_{i,j} = \frac{1}{\sqrt{\beta}}\left(\sqrt{(\Delta\mathbf{p}_i + \mathbf{R}_{z,\psi}\bar{\mathbf{d}}_j)^T(\Delta\mathbf{p}_i + \mathbf{R}_{z,\psi}\bar{\mathbf{d}}_j)} - \sqrt{(\Delta\mathbf{p}_i)^T(\Delta\mathbf{p}_i)} + \epsilon_{\delta,i,j}\right) \tag{11}$$

where $\Delta\mathbf{p}_i = \mathbf{p}^n - \breve{\mathbf{p}}^n_i = [\Delta x_i, \Delta y_i, \Delta z_i]^T$ and $\bar{\mathbf{d}}_j = \mathbf{R}_{y,\theta}\mathbf{R}_{x,\phi}\mathbf{d}^b_j = \left[\bar{d}_{j,x}, \bar{d}_{j,y}, \bar{d}_{j,z}\right]^T$, with $\mathbf{R}_{y,\theta}$ and $\mathbf{R}_{x,\phi}$ given from the calculated ϕ and θ. Squaring (11), omitting measurement noise for simplicity and performing some algebraic manipulation gives

$$(\Delta\mathbf{p}_i + \mathbf{R}_{z,\psi}\bar{\mathbf{d}}_j)^T(\Delta\mathbf{p}_i + \mathbf{R}_{z,\psi}\bar{\mathbf{d}}_j) = \beta\delta^2_{i,j} + 2\sqrt{\beta}\delta_{i,j}||\Delta\mathbf{p}_i|| + (\Delta\mathbf{p}_i)^T(\Delta\mathbf{p}_i) \tag{12}$$

By describing $\mathbf{R}_{z,\psi}$ as

$$\mathbf{R}_{z,\psi} = \begin{bmatrix} \cos(\psi) & -\sin(\psi) & 0 \\ \sin(\psi) & \cos(\psi) & 0 \\ 0 & 0 & 1 \end{bmatrix} = \begin{bmatrix} x_1 & -x_2 & 0 \\ x_2 & x_1 & 0 \\ 0 & 0 & 1 \end{bmatrix} \tag{13}$$

it is possible to estimate $\mathbf{R}_{z,\psi}$ using the least squares approach, thus giving a measurement of $\mathbf{d}^n_j$ which can be used in a Kalman Filter (KF), described in Sec. III-B. With $\mathbf{R}_{z,\psi}$ as in (13), the set of equations can be written as

$$2\left[\bar{d}_x\Delta x_i + \bar{d}_y\Delta y_i, \bar{d}_x\Delta y_i - \bar{d}_y\Delta x_i\right] \cdot [x_1, x_2]^T = \beta\delta^2_{i,j} + 2\sqrt{\beta}\delta_{i,j}||\Delta\mathbf{p}_i|| - ||\mathbf{d}_j||^2 - \bar{d}_z\Delta z_i \tag{14}$$

By stacking all measurements, it is possible to write

$$\mathbf{A}\mathbf{x} = \mathbf{z} \tag{15}$$

where $\mathbf{x} = [x_1, x_2]^T$

$$\mathbf{A} = 2\begin{bmatrix} \bar{d}_{1,x}\Delta x_1 + \bar{d}_{1,y}\Delta y_1, \bar{d}_{1,x}\Delta y_1 - \bar{d}_{1,y}\Delta x_1 \\ \vdots \\ \bar{d}_{M,x}\Delta x_N + \bar{d}_{M,y}\Delta y_N, \bar{d}_{M,x}\Delta y_N - \bar{d}_{M,y}\Delta x_N \end{bmatrix}$$

$$\mathbf{z} = \begin{bmatrix} \beta\delta^2_{1,1} + 2\sqrt{\beta}\delta_{1,1}||\Delta\mathbf{p}_1|| - ||\mathbf{d}_1||^2 - \bar{d}_{1,z}\Delta z_1 \\ \vdots \\ \beta\delta^2_{N,M} + 2\sqrt{\beta}\delta_{N,M}||\Delta\mathbf{p}_N|| - ||\mathbf{d}_M||^2 - \bar{d}_{M,z}\Delta z_N \end{bmatrix}$$

If Assumption 1 is fulfilled, at least three TDOA measurements are available, and the sender positions are not co-linear in the north-east-plane (NE-plane), $\mathbf{A}$ will have full rank, and it is possible to solve (15) as a least squares problem. When $\mathbf{R}_{z,\psi}$ is calculated from solving (15), a measurement of $\mathbf{d}^n_j$

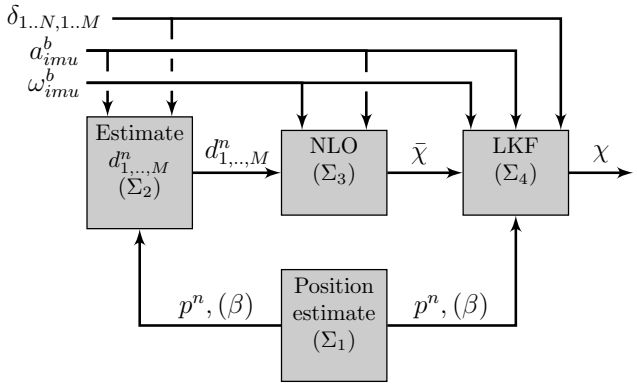

Fig. 2: Filter structure. The output β from the "Position estimate"-block can be omitted if it is not available.[20]

can be constructed from $\mathbf{d}^n_j = \mathbf{R}_{z,\psi}\bar{\mathbf{d}}_j$. The vectors are also normalized to have unit length.

As mentioned in Sec. II-D, it is possible to calculate $\mathbf{d}^n_{1,..,M}$ without estimates of roll angle and pitch angle. This could be done by simply viewing each vector as the unknown and applying a similar approach as above. However, this will usually result in a less accurate attitude estimate, depending on the accuracy of the TDOA measurements compared to the accelerometer measurements.

III. ATTITUDE AND RATE SENSOR BIAS FILTER

Attitude and rate sensor bias filter applied in the experiments is based on the XKF-principle, in which a globally stable, auxiliary estimator provides a linearization point for a LKF. The overall structure of the suggested filter is shown in Fig. 2. As can be seen from Fig. 2, there are no feedback loops, making stability analysis a question of the model in the LKF being uniformly completely observable (UCO) and uniformly completely controllable (UCC)[17]. This is in contrast to the EKF, in which stability has not been proven for the model used, due to the feedback where the estimated state itself is used as a linearization point for the filter. This increases the complexity of potentially proving stability for the EKF significantly. Stability for the suggested filter is discussed in Sec. III-D1. In the following each subsystem will be described in more detail.

We define $\mathbf{I}_i$ as a $i\,x\,i$ identity matrix, $\mathbf{0}_i$ as a $i\,x\,i$ matrix of zeros and $\mathbf{0}_{i\,x\,j}$ as a $i\,x\,j$ matrix of zeros .

A. Subsystem Σ_1: Position Estimate

The position estimate is provided by a simplified version of the filter suggested in [19]. This filter is also built on the XKF principle, and takes pseudo-range-, depth- and acceleration-measurements as input, giving position, velocity and scaling factor for underwater wave speed (β in eq. (4)) as an output. The filter consists of three stages, in which the first stage is an algebraic transformation converting pseudo-range- and depth-measurements into position and scaling factor measurements, the second stage is a linear KF taking these measurements as input and the third is a LKF using the original pseudo-range- and depth-measurements as input, employed to increase accuracy. From both simulations and lab testing it seems the accuracy requirements for the position estimate are met after just employing the first two stages. Consequently, with regards to computational complexity, the output from the second stage is used as the position estimate in the filter in this paper. Naturally, the full filter can be used in a different scenario if necessary, due to increased measurement noise or changed sender geometry.

As the acceleration measurements require an attitude estimate to be rotated to the NED frame, and the purpose of this paper is to estimate attitude, acceleration measurements are not employed in the position estimate filter. This also significantly reduces the computational burden, as the filter only needs to be updated each time pseudo-range measurements arrive, in other words at a frequency of approximately 1.5 Hz.

The KF is based on the system model

$$\dot{\mathbf{p}}^n = \mathbf{v}^n$$
$$\dot{\beta} = \varepsilon_\beta$$
$$\dot{\mathbf{v}}^n = \varepsilon_a$$

or, written in matrix form

$$\dot{\chi}_p = \begin{bmatrix} \mathbf{0}_3 & 0 & \mathbf{I}_3 \\ \mathbf{0}_3 & 0 & \mathbf{0}_3 \\ \mathbf{0}_3 & 0 & \mathbf{0}_3 \end{bmatrix} \chi_p + \begin{bmatrix} 0 & \mathbf{0}_3 \\ 1 & \mathbf{0}_3 \\ 0 & \mathbf{I}_3 \end{bmatrix} \begin{bmatrix} \varepsilon_\beta \\ \varepsilon_a \end{bmatrix} \tag{16}$$

with measurement

$$\mathbf{y} = \begin{bmatrix} \mathbf{I}_4 & \mathbf{0}_{4x3} \end{bmatrix} \chi_p + \varepsilon_{y_p} \tag{17}$$

where $\mathbf{v}^n$ is the velocities in the NED frame and $\chi_p = \left[\mathbf{p}^{n\,T}, \beta, \mathbf{v}^{n\,T}\right]^T$ is the full state vector. ε_β, ε_a are the process noises with variance σ^2_β and covariance matrix $\mathbf{Q}_a$ respectively. The covariance matrix of ε_{y_p} is approximated by first order linearization and employing finite differences using the central differences approach and the values of $\sigma^2_{y,i}$ and σ^2_z.

1) Outlier Detection: The position estimate filter is also responsible for performing outlier detection for the range measurements. Outliers occured during testing, and a simple outlier detection scheme based on the Mahalanobis distance seemed sufficient. The Mahalanobis distance is given by[3]

$$d_M = \nu_k^T \mathbf{S}^{-1} \nu_k \tag{18}$$

where $\nu_k = y_i - \hat{y}_i$ and $\mathbf{S} = \mathbf{H}_{k,i}\mathbf{P}_{k+1/k}\mathbf{H}^T_{k,i} + \sigma^2_{y,i}$ is the filter innovation covariance. $\mathbf{H}_{k,i}$ is the Jacobian of (4) for measurement i. d_M is calculated for each pseudo-range measurement, and a measurement is rejected if d_M is above a given threshold, γ_M.

As each pseudo-range difference measurement requires two different pseudo-ranges, from two receivers, one position

estimate filter is run for each receiver. For the base receiver the position estimate is used, as described in Sec. II-E, and for the other receivers the filter is solely run for the purpose of outlier detection. Consequently, less computationally demanding outlier detection approaches can be employed for other receivers than the base receiver. However, as mentioned above, these filters need only be run with the same frequency as the TDOA measurements, in this case approximately 1.5 Hz.

B. Subsystem Σ_2: Estimate Vectors Between Receivers, $\mathbf{d}^n_{1,..,M}$

This subsystem performs the calculation of $\mathbf{d}^n_{1,..,M}$ from TDOA measurements, roll angle, pitch angle and position estimates as described in Sec. II-E. However, the solutions for $\mathbf{d}^n_{1,..,M}$ can be noisy due to the fact that measurement noise is not taken into account when performing the calculations. As a result of this, a KF is used to filter the data before they are used as input for the NLO.

The calculated $\mathbf{d}^n_{1,..,M}$ as described in Sec. II-E is used as input for a Kalman filter with model given by

$$\begin{aligned} \dot{\mathbf{d}}^n_j &= \mathbf{a}^n_j \\ \dot{\mathbf{a}}^n_j &= \epsilon_d \\ \mathbf{y}_d &= \mathbf{d}^n_j + \epsilon_y \end{aligned} \tag{19}$$

where ϵ_d and ϵ_y are zero-mean Gaussian white noise vectors and $\mathbf{y}_d$ is the calculated measurement of $\mathbf{d}^n_j$. The covariance matrix of ϵ_d, $\mathbf{Q}_d$ is tuned based on expected rate of change in attitude for the vehicle and the covariance matrix of ϵ_y, $\mathbf{R}_d$ can be calculated from the finite differences approach, combined with the values of $\sigma^2_{\delta,i,j}$ and ϵ_a.

It would also be possible to apply less computationally expensive methods to filter the data, for example a band-pass filter or a low-pass filter. However, the noise in the input of each part of $\mathbf{d}^n_j$ are not independent of each other due to the fact that they are calculated from the same measurements. Furthermore, the characteristics of the noise are dependent on the characteristics of $\mathbf{A}$ and $\mathbf{z}$ in eq. (15), which are dependent on both sender and receiver position. This dependency is similar to dilution of precision (DOP)[22], which is commonly used in GPS positioning, and more specifically the attitude dilution of precision discussed in [27]. As a result of this the noise characteristics will change with vehicle position, and a KF with the model given in eq. (19) can be viewed as a band-pass filter with position-dependent cut-off frequencies. Both cut-off frequencies and dependencies between the measurements are approximated by employing the finite differences approach for $\mathbf{R}_d$.

C. Subsystem Σ_3: Non-linear Observer

As the purpose of the NLO is to provide a globally stable estimate of attitude and rate sensor bias, with vector- and rate sensor measurements as input, any NLO that performs this action can be employed. The NLO used in this paper is suggested in Grip et al.[12], which provides an estimate of the attitude described by a $3\,x\,3$ matrix asymptotically converging towards a rotational matrix, and the rate sensor bias. This NLO is globally exponentially stable (GES) except for a singularity point if Assumption 1 is fulfilled, along with a known upper bound for the bias and a design property regarding the matrices $\mathbf{A}^n_j(t)$ and $\mathbf{A}^b_j(t)$ used in the estimator. The observer equations are given by

$$\dot{\hat{\mathbf{R}}} = \hat{\mathbf{R}}\mathbf{S}(\omega^b_{imu} - \hat{\mathbf{b}}) + \sigma\mathbf{K}_p\mathbf{J}(t,\hat{\mathbf{R}}) \tag{20}$$

$$\dot{\hat{\mathbf{b}}} = \mathrm{Proj}(\hat{\mathbf{b}}, -k_I \mathrm{vex}(\mathbb{P}_\mathrm{a}(\hat{\mathbf{R}}^T_S\mathbf{K}_p\mathbf{J}(t,\hat{\mathbf{R}})))) \tag{21}$$

$$\mathbf{J}(t,\hat{\mathbf{R}}) = \sum_{j=1,..,q} (\mathbf{A}^n_j(t) - \hat{\mathbf{R}}\mathbf{A}^b_j(t))\mathbf{A}^b_j(t)^T \tag{22}$$

where $k_I > 0$ is a scalar tuning parameter, $\mathbf{K}_p > 0$ is a symmetric gain matrix, $\sigma \geq 1$ is a scaling factor to achieve stability and $\mathbf{A}^n_j(t)$ and $\mathbf{A}^b_j(t)$ are designed to fulfill certain properties, in this case chosen like in [12] for two vectors:

$$\mathbf{A}^\iota_1 = \begin{bmatrix} \frac{\mathbf{w}^\iota_1}{||\mathbf{w}^\iota_1||} & \frac{\mathbf{S}(\mathbf{w}^\iota_1)\mathbf{w}^\iota_2}{||\mathbf{S}(\mathbf{w}^\iota_1)\mathbf{w}^\iota_2||} & \frac{\mathbf{S}^2(\mathbf{w}^\iota_1)\mathbf{w}^\iota_2}{||\mathbf{S}^2(\mathbf{w}^\iota_1)\mathbf{w}^\iota_2||} \end{bmatrix}$$

where $\iota \in \{n, b\}$, and $\mathbf{A}^\iota_2$ follows the same formula, but with the vectors reversed. $\mathbf{S}(\mathbf{x})$ is a skew-symmetric matrix such that for any $\mathbf{y} \in \mathbb{R}^3$, $\mathbf{S}(\mathbf{x})\mathbf{y} = \mathbf{x} \times \mathbf{y}$, $\mathrm{vex}(\mathbf{S}(\mathbf{x})) = \mathbf{x}$, $\mathbb{P}_\mathrm{a}(\mathbf{X}) = \frac{1}{2}(\mathbf{X} - \mathbf{X}^T)$ and $\hat{\mathbf{R}}_s = \mathrm{sat}_1(\hat{\mathbf{R}})$, the element-wise saturation function of $\hat{\mathbf{R}}$. Proj is a projection function ensuring that the bias stays within a pre-defined upper bound, given by

$$\mathrm{Proj}(\hat{\mathbf{b}}, \beta) = \begin{cases} \left(\mathbf{I}_3 - \frac{c(\hat{\mathbf{b}})}{||\hat{\mathbf{b}}||^2}\hat{\mathbf{b}}\hat{\mathbf{b}}^T\right)\beta, & ||\hat{\mathbf{b}}|| \geq M_b,\ \hat{\mathbf{b}}^T\beta > 0, \\ \beta, & \text{otherwise,} \end{cases}$$

where $c(\hat{\mathbf{b}}) = \min\left\{1, (||\hat{\mathbf{b}}||^2 - M_b^2)/(M_b^2 - M_b)\right\}$. For further details and stability proof, see Grip et al.[12].

As mentioned above, the inputs to the NLO are rate sensor measurements in addition to vectors that are known in one coordinate frame and measured in the other. In the case of this paper, the input will be $M+1$ vectors, more specifically the acceleration measurement where gravity is assumed to be be dominating factor and M vectors between receivers, known in the body frame and calculated in the NED-frame from the approach described in Sec. II-E and Sec. III-B. As the sampling frequencies of the accelerometer (approximately 100 Hz) is very different from the TDOA measurements (approximately 1.5 Hz), $\mathbf{K}_p$ is chosen to be ten times larger when TDOA measurements are available, $\mathbf{K}_{pTDOA} = 10\mathbf{K}_p$.

It is desired in the NLO to have both fast convergence and stable stationary performance. Choosing large gains gives fast convergence, but will give a more aggressive estimator, resulting in amplification of measurement noise. Therefore it is natural to have large gains in the start, when the estimator is converging, and turn down the gains when the estimator is assumed to have converged. Consequently, both $\mathbf{K}_p$ and k_I in the observer are set to be five times the chosen values for the first 20 seconds of running the filter.

The output from the chosen NLO is a rotation matrix and rate sensor bias. As the states chosen for the filter are Euler angles and rate sensor bias, the rotation matrix is converted into Euler angles before it is given as output. The total output of the NLO is the Euler angles linearization point, $\bar{\mathbf{\Theta}}$ and the rate sensor bias linearization point, $\bar{\mathbf{b}}$, combined in the vector $\bar{\chi} = \begin{bmatrix} \bar{\mathbf{\Theta}}^T & \bar{\mathbf{b}}^T \end{bmatrix}^T$.

D. Subsystem Σ_4: Linearized Kalman Filter

The LKF is based on linearizing the system model about the linearization point from Σ_3, $\bar{\chi}$. The model used in the LKF is given by

$$\dot{\chi} = \begin{bmatrix} \mathbf{0}_3 & -\mathbf{T}(\bar{\chi}) \\ \mathbf{0}_3 & \mathbf{0}_3 \end{bmatrix} \chi + \begin{bmatrix} \mathbf{T}(\bar{\chi}) \\ \mathbf{0}_3 \end{bmatrix} \omega_{b/n}^b + \begin{bmatrix} \mathbf{T}(\bar{\chi}) & \mathbf{0}_3 \\ \mathbf{0}_3 & \mathbf{I}_3 \end{bmatrix} \epsilon_\chi \tag{23}$$

where $\epsilon_\chi = \begin{bmatrix} \epsilon_\omega & \epsilon_b \end{bmatrix}^T$ is a vector of two zero-mean Gaussian white noise vectors with covariances $\mathbf{Q}_\omega$ and $\mathbf{Q}_b$ and $\mathbf{T}$ is derived in Fossen[9], given by

$$\mathbf{T} = \begin{bmatrix} 1 & s\phi t\theta & c\phi t\theta \\ 0 & c\phi & -s\phi \\ 0 & s\phi/c\theta & c\phi/c\theta \end{bmatrix} \tag{24}$$

where $s\cdot = \sin(\cdot)$, $c\cdot = \cos(\cdot)$ and $t\cdot = \tan(\cdot)$, and

$$\chi = \begin{bmatrix} \mathbf{\Theta} \\ \mathbf{b} \end{bmatrix}$$

The measurement equation is given by

$$\mathbf{y}_{LKF} = \mathbf{h}(\chi) = \begin{bmatrix} \phi \\ \theta \\ \delta_{1,1} \\ \vdots \\ \delta_{N,M} \end{bmatrix} + \epsilon_h \tag{25}$$

where ϵ_h is a vector of zero-mean Gaussian white noise with covariance $\mathbf{R}_h$, ϕ and θ are calculated from (7) and (8). As $\mathbf{h}(\chi)$ is a non-linear function wrt. χ, it is necessary to perform a linearization for approximating $\hat{\mathbf{y}}_{LKF}$ about $\bar{\chi}$. The first order Taylor-series approximation of (25) about the linearization point $\bar{\chi}$ is given by

$$\hat{\mathbf{y}}_{LKF} \approx \mathbf{h}(\bar{\chi}) + \left.\frac{\mathrm{d}\mathbf{h}(\chi)}{\mathrm{d}\chi}\right|_{\chi=\bar{\chi}} (\chi - \bar{\chi})$$

As can be seen in (24), the filter has a singularity when $\theta = \pm\frac{\pi}{2}$. This is a widely known drawback of using Euler angles. However, these singularities are well known and therefore it is easily detectable if the filter is close to one of the singularities. As is mentioned in [9], if the filter is close to one of the singularities, the Euler angle representation can be changed to a representation which has different singularities far from the current working point. The models for these alternative representations have not been considered as the approaches are very similar to the one suggested in this paper. The problem of getting close to the singularities was never an issue during testing as the equilibrium state of the ROV is $\phi = \theta = 0$.

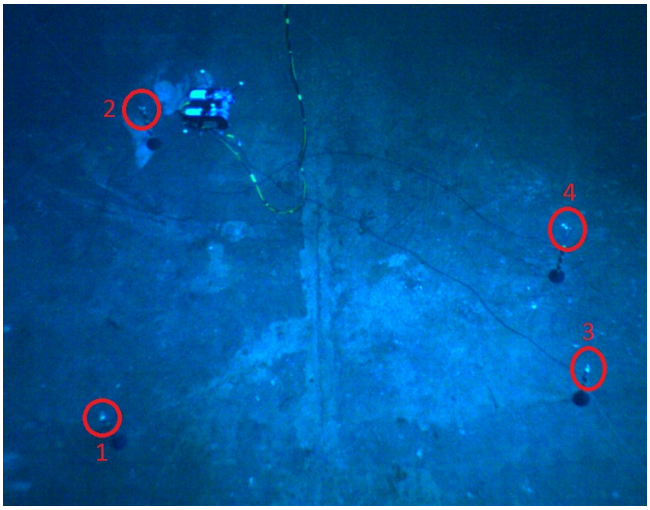

Fig. 3: Senders and ROV during testing

1) Stability Analysis: For a detailed stability analysis, see [20]. The model given above is shown to be UCO and UCC, and does therefore inherit stability properties from the NLO in Σ_3, which is GES. However, as there are singularities in the model at $\theta = \pm\pi/2$, the filter is GES except for the singular points. In practice this is a minor problem, as the singularities are known, easily detectable and as mentioned it is possible to switch between Euler angle representations if needed.

IV. System Setup, Calibration and Implementation Aspects

The experiments were performed in LabOceano at the Federal University of Rio de Janeiro. Due to limitations in the ground truth measurement system, the ROV had to stay inside a designated area of around $8\,\mathrm{m} \times 8\,\mathrm{m} \times 8\,\mathrm{m}$. However, this is sufficient to give an experimental validation of the filter, as the important factor for accuracy is the co-linearity of each vector from senders to receiver, and not the distance between senders and receiver. This will be further discussed in Sec. VI.

A. System setup

The acoustic system used is a development kit provided by Waterlinked[2], consisting of four senders and four receivers. Waterlinked specializes in short-range, accurate postitioning for underwater vehicles. The intended use of the Waterlinked system is accurate state estimation within a small area of up to $100\,\mathrm{m} \times 100\,\mathrm{m}$. Four senders were placed on the seabottom at 13-14 m depth, see Fig. 3 for an image of the sender setup.

The ROV used is the BlueROV2[1], and four receivers were placed on the ROV with a custom made rack for increasing the distance between receivers, see Fig. 4 for an image. However, for simplicity, only two receivers were used in the experiment as this was enough to give experimental validation of the filter. Employing more receivers might increase accuracy, but

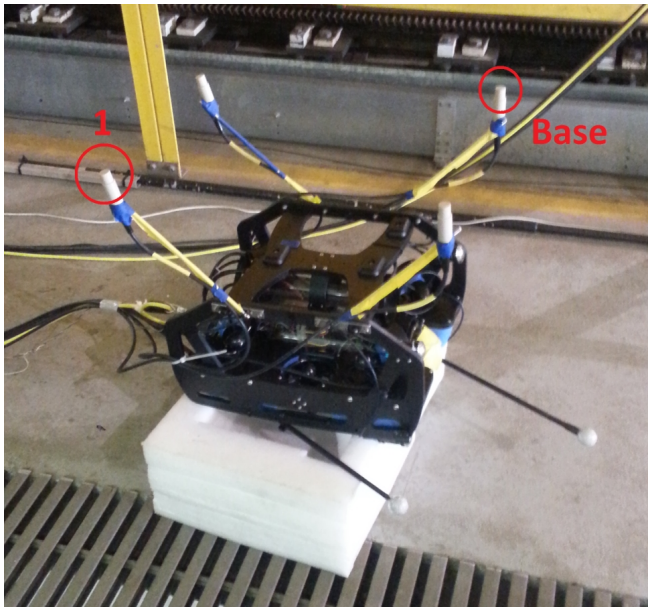

Fig. 4: ROV with receiver setup. In the image the ROV is upside down. Base receiver and receiver 1 are marked

in the authors opinion it is also important to demonstrate that two receivers is sufficient. The IMU used is the internal IMU in the M Robotics PixHawk autopilot controller, a microelectromechanical IMU with a price of less than 20$, which is in the lower part of the IMU price/quality range. The IMU data is read with a frequency of approximately 100 Hz, and pseudo-range measurements are run with a frequency of approximately 1.5 Hz.

For ground truth measurements, a Qualisys underwater camera positioning system with measurement frequency of approximately 50 Hz is employed, giving 6 degree-of-freedom (DOF) measurements of the ROV, with stated millimeter precision for position and sub-degree precision on the attitude. However, this is under optimal circumstances, and during testing some inaccuracies in attitude of up to two degrees were registered. This will be discussed further in Sec. V.

B. Calibration

There are several sources of error and inaccuracy in this system, and different calibration schemes have been applied to try to take this into account.

For a description of possible IMU error sources, see [10]. As the accelerometer is only used for calculating roll angle and pitch angle, it is assumed the rotational offset is the most important offset, whereas scaling of measurements and size of the gravity vector are less interfering. The accelerometer bias can cause an offset in the roll angle and pitch angle calculations if it is large enough, but only compensating for rotational offset seemed to give sufficient accuracy. The rotational offsets between the Qualisys body coordinate frame and the IMU body coordinate frame, as well as the rotational offset between the Qualisys world frame and the inertial NED frame were estimated by running a nonlinear optimization scheme, minimizing the error between the extracted roll angle and pitch angle data from Qualisys with the roll angle and pitch angle data computed by the accelerometer measurements.

Parameter	$\breve{p}_1^n$	$\breve{p}_2^n$	$\breve{p}_3^n$	$\breve{p}_4^n$	d_1^b
x[m]	-6.86	-6.83	-1.19	-1.41	-0.544
y[m]	1.04	-3.21	0.531	-1.10	-0.375
z[m]	0.357	0.506	0.338	-0.130	-0.0113

TABLE I: Calibration results

For calibrating sender positions, a nonlinear optimization scheme minimizing the error between the calculated geometric range using Qualisys and the measured ranges was applied. Furthermore, for calibrating receiver positions in the body frame and logger time delay, a nonlinear optimization scheme was also applied, minimizing the error between the calculated geometric range differences based on Qualisys data and the measured range differences.

The results from the calibration can be seen in Tab. I .

C. Implementation Aspects

The IMU measurement frequency was approximately 100 Hz, high enough to capture the dynamics of the system, whereas a higher frequency would result in a larger computational burden. First order Euler approximation has been used as the integration scheme for all subsystems, as this seemed sufficient to achieve desired accuracy. As the filters integrate the IMU data, the frequency of the filters is the same as the frequency of the IMU data, approximately 100 Hz, resulting in small timesteps compared to the dynamics of the system, thus lessening the need for a more extensive scheme.

1) Range Measurement Timing Issues: As mentioned in Sec. II-E, at least three TDOA-measurements must be available before being able to calculate the vectors between receivers, $\mathbf{d}^n_{1,..,M}$ in Σ_2. As the distances between sender and receiver in the experiment are small (maximum $8\,\mathrm{m}$) and the acoustic waves are sent at the same time, the time offsets between the arrival of each acoustic wave are assumed to be negligible in the experiments performed in this paper. However, in a setup with larger distances between sender and receiver, the waves will arrive at significantly different times, and this needs to be handled in the filter. For calculating $\mathbf{d}^n_{1,..,M}$ the simplest way of handling an offset in arrival time from each transponder is to simply wait until three or more waves have arrived, and then start the calculations. Naturally this will decrease accuracy, as it is assumed when doing the calculations that this is an instant measurement with no time offset.

A more extensive approach might be to take the vehicle position into account after the position filter, Σ_1, has converged, and in this way be able to identify lost measurements

by knowing the expected time for a measurement from a given position to arrive. The accuracy of this scheme is dependent on several factors, such as position estimate accuracy, magnitude of time offset, probability of a lost measurement and vehicle velocity. However, it is important to note that simulations done in [17][20][19] indicate that in general for the XKF the linearization point provided by the auxiliary estimator can be somewhat inaccurate, depending on system configuration and noise magnitude, and the output of the filter will still be close-to-optimal wrt. noise.

In the LKF in Σ_4, handling measurement time offset is fairly straight forward, as each measurement can be applied when it arrives, simply by modifying the measurement equation, (25), to only take the received measurement.

Each acoustic wave needs to be received, registered and processed to be used as a pseudo-range measurement. This results in a natural time-delay for each measurement. As the data in this case has been post-processed, a simple time offset for all measurements has been added to take this into account, but in a real-time system, ways of handling this delay must be applied, see for example [8][15].

2) Handling Outliers: Handling outliers is performed the same way as handling lost measurements. As mentioned above, at least three valid TDOA measurents are needed to calculate $\mathbf{d}^n_{1,..,M}$ in Σ_2. Consequently, if less than three measurements are found to be valid, this stage is simply avoided at the given time, and the system waits for new measurements. For the LKF in Σ_4 any number of valid measurements can be applied, by modifying (25).

3) Computational Load: As subsystems Σ_1 and Σ_2 are run only when pseudo-range measurements are received, approximately 1.5 Hz, the main computational load is in Σ_3 and Σ_4. The state in Σ_3 and Σ_4 must be updated each time an IMU-measurement arrives, in other words these two subsystems are run at the same frequency as the IMU data is extracted, approximately 100 Hz. When pseudo-range measurements are available, Σ_4 contains more complex calculations, especially matrix inversions, whereas Σ_3 is mostly multiplication. As this only happens approximately every $0.67\,\mathrm{s}$, the total computational load of Σ_3 and Σ_4 is similar, and the computational load for the full filter was around 2.35 times more than running an EKF for the given setup and measurement frequencies. However, if the filter in [19] is run for accurate positioning also in a full state estimation scheme, the computational burden of Σ_1 can be disregarded as Σ_1 needs to be run for the position filter regardless. Then the computational load of the suggested filter is around 2 times more than running an EKF.

V. TESTING AND RESULTS

Two experiments, A and B, have been performed, to cover two types of common ROV manoeuvres. In experiment A the ROV is almost stationary, only turning from side to side, changing the yaw angle similar to an inspection scenario. During experiment B the ROV is driving back and forth, similar to a transit scenario.

Assuming both bias and vehicle acceleration are negligible compared to the gravity vector gave satisfactory results. Consequently, in the experiments it is assumed $\mathbf{a}^b_{imu} \approx \mathbf{R}^b_n \mathbf{g}^n + \epsilon_a$, see Sec. II-C for discussion.

Simulations and experiences with real lab data suggest that all subsystems Σ_1 - Σ_4 are robust towards inaccurate initial values, and to observe both transient and stationary behaviour, the initial estimates for each filter, especially in yaw angle are rather inaccurate. Each parameter has been decided through trial and error, by considering the expected rate of change for different parts of the system, and looking at the noise in the measured data. The tuning parameter values for each subsystem can be seen in Tab. II. $\mathbf{P}_0$ is the initial covariance matrix for the KFs, $\mathbf{x}_0$ is the initial estimate for each subsystem and $\mathbf{k}_{i\,x\,j}$ means an i times j matrix with containing the value $\mathbf{k}$. $\mathrm{diag}(\mathbf{v})$ is a diagonal matrix with the vector $\mathbf{v}$ along the diagonal.

For comparison, an EKF is also run, with the same tuning as the LKF in Σ_4, the only difference being that the linearization point is the estimated state, and not the output from Σ_3. The output from the EKF is denoted χ_{EKF}. Furthermore, an LKF using the ground truth states instead of the output from Σ_3 as linearization point is also run. This is a non-implementable filter in a real scenario, as ground truth measurements are not available, but it is interesting to give an impression of the optimal filter performance for the current scenario and tuning. This filter is also tuned the same way as the LKF in Σ_4, and the output from this filter is denoted χ_{opt}.

A. Experiment A: Turning

In this experiment the ROV is fairly stationary with a constant depth, rotating from side to side with different angular velocity, with yaw angles of around $-\frac{\pi}{2} \leq \psi \leq \frac{\pi}{2}$. The ground truth position and Euler angles from the Qualisys system can be seen in Fig. 5.

The raw pseudo-ranges measured can be seen in Fig. 6. Throughout experiment A around $0.53\,\%$ of the pseudo-range measurements were rejected as outliers. The estimated and ground truth value of $\mathbf{d}^n_1$ is shown in Fig. 7, and the real and estimated position is shown in Fig. 8. The estimated rate sensor bias is shown in Fig. 9, and the Euler angle errors are shown in Fig. 10, with two different axis to show transient and stationary behaviour. No error plot is shown for the estimated rate sensor bias, as it is difficult to know this in reality, but at the end of the experiment the estimated rate sensor bias was $\mathbf{b}_{XKF} = \left[4.6 \cdot 10^{-4}, 5.0 \cdot 10^{-3}, -5.2 \cdot 10^{-3}\right]^T$ whereas in calibration this bias was found to be $\mathbf{b}_{cal} = \left[7.0 \cdot 10^{-4}, 5.3 \cdot 10^{-3}, -5.0 \cdot 10^{-3}\right]^T$, which is similar considering the magnitude of the bias compared to the expected rate sensor measurement noise, stated as $\mathbf{Q}_\omega$ in Tab. IId.

Parameter	σ_β^2	$\mathbf{Q}_a$	$\sigma_{y,i}^2$
Value	$(1 \cdot 10^{-3})^2$	$0.5^2 \cdot \mathbf{I}_3$	0.02^2

Parameter	γ_M	$\mathbf{x}_0$	$\mathbf{P}_0$
Value	3	$\begin{bmatrix} \mathbf{0}_{3x1} \\ 1 \\ \mathbf{0}_{3x1} \end{bmatrix}$	$\text{diag}(\begin{bmatrix} \mathbf{5}_{3x1}^2 \\ \mathbf{0.1}_{4x1}^2 \end{bmatrix})$

(a) Values for Σ_1

Parameter	$\mathbf{Q}_d$	$\sigma_{\delta,i,j}^2$	ϵ_a
Value	$3^2 \cdot \mathbf{I}_3$	0.05^2	0.3^2

Parameter	$\mathbf{x}_0$	$\mathbf{P}_0$	
Value	$\mathbf{0}_{6x1}$	$\text{diag}(\mathbf{0.5}_{6x1})$	

(b) Values for Σ_2

Parameter	k_I	K_p	σ
Value	0.05	$\mathbf{I}_3$	1

Parameter	M_b	$M_{\hat{b}}$	$\mathbf{x}_0$
Value	0.39	0.4	$\begin{bmatrix} 0.1 \\ 0.1 \\ \pi/2 \\ \mathbf{0}_{3x1} \end{bmatrix}$

(c) Values for Σ_3

Parameter	$\mathbf{Q}_\omega$	$\mathbf{Q}_b$	$\mathbf{R}_h$
Value	$0.05^2 \cdot \mathbf{I}_3$	$\left(1 \cdot 10^{-4}\right)^2 \cdot \mathbf{I}_3$	$\text{diag}([\mathbf{0.1}_{6x1}^2])$

Parameter	$\mathbf{x}_0$	$\mathbf{P}_0$	
Value	$\begin{bmatrix} 0.1 \\ 0.1 \\ \pi/2 \\ \mathbf{0}_{3x1} \end{bmatrix}$	$\text{diag}(\begin{bmatrix} \mathbf{1}_{3x1}^2 \\ \mathbf{0.1}_{3x1}^2 \end{bmatrix})$	

(d) Values for Σ_4

TABLE II: Tuning parameter values

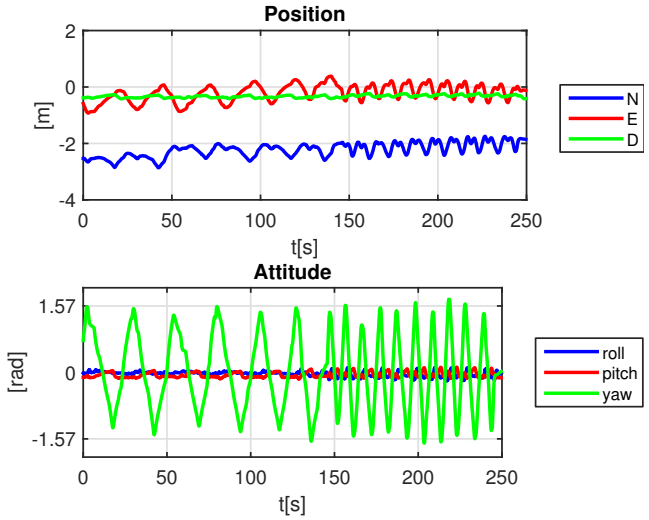

Fig. 5: Experiment A: Ground truth position and Euler angles from the Qualisys system

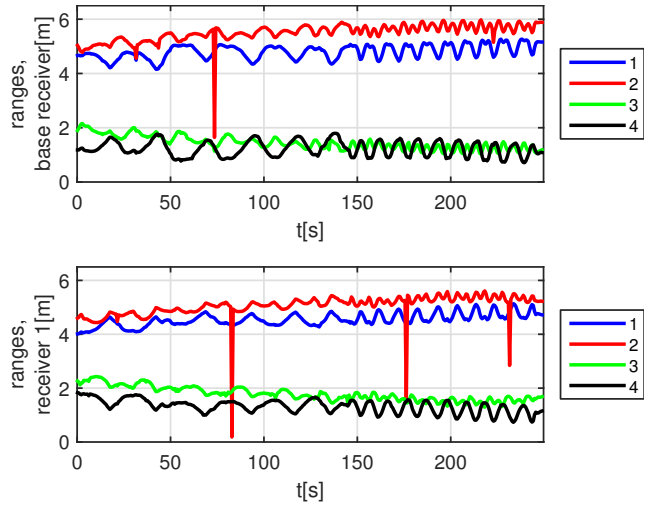

Fig. 6: Experiment A: Raw measured pseudo-ranges for both receivers. Pseudo-range i is the range measured from the sender at $\breve{\mathbf{p}}_i^n$.

It is apparent that the error for the linearization point, $\bar{\chi}$, is larger than the error for the output of the three other filters, which have similar response (although the EKF has a slightly larger transient error). This fits well with the theory and reasoning for the XKF principle, as the NLO is designed for global stability, not for optimal performance wrt. measurement noise whereas the LKF is designed to be close-to-optimal wrt. noise, given that the linearization point is accurate, and the system is modeled correctly. Consequently, the LKF improves the estimate of the NLO by having a more accurate model of the system providing a filter which is statistically optimal, and using the output of the NLO simply as a linearization point.

As can be seen from the results, the filter converges quickly, and stays close to the ground truth values. The RMSE for roll angle, pitch angle and yaw angle after convergence for the different filters is shown in Tab. III. However, this RMSE is most likely a combination of estimator and ground truth error, as will be discussed in the following paragraph. Note that the RMSE of the suggested filter is equal to the optimal filter, supporting the claim that the suggested filter is close-to-optimal wrt. noise.

The roll angle and pitch angle errors have some spikes , especially for $150\,\text{s} < t < 250\,\text{s}$. By looking at the ground truth attitude data for the times of these spikes, it seems this is a result of inaccuracies in ground truth, as the ground truth attitude jumps back and forth at the times of these spikes (see Fig. 11 for an illustration). Furthermore, for the roll angle estimate there is a larger error when the vehicle is turning quicker. This might be due to the fact that the IMU is not in the center of gravity, thus resulting in measured accelerations

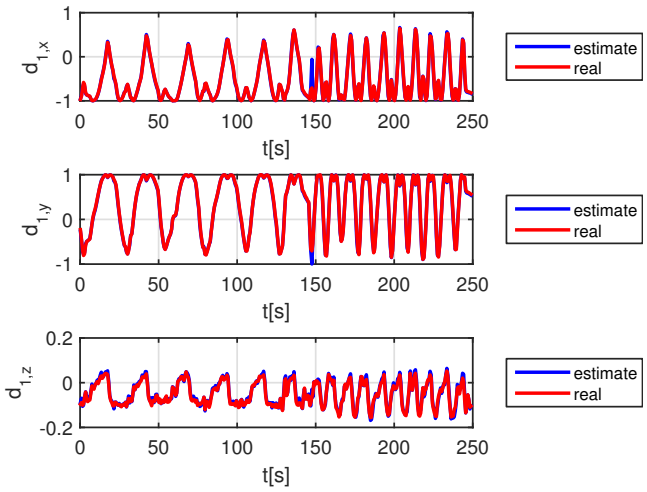

Fig. 7: Experiment A: Real and estimated values for $\mathbf{d}_1^n = [d_{1,x}, d_{1,y}, d_{1,z}]^T$

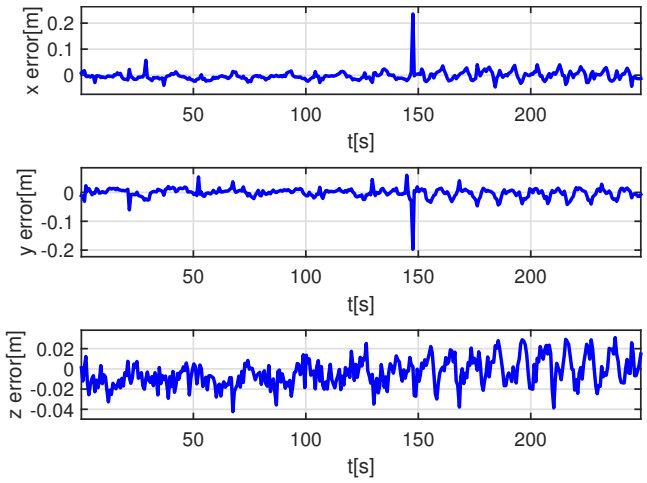

Fig. 8: Experiment A: Position estimation errors

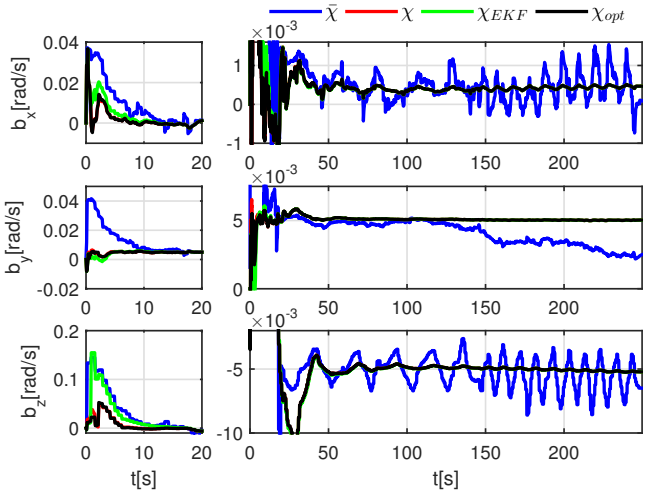

Fig. 9: Experiment A: Estimated rate sensor bias

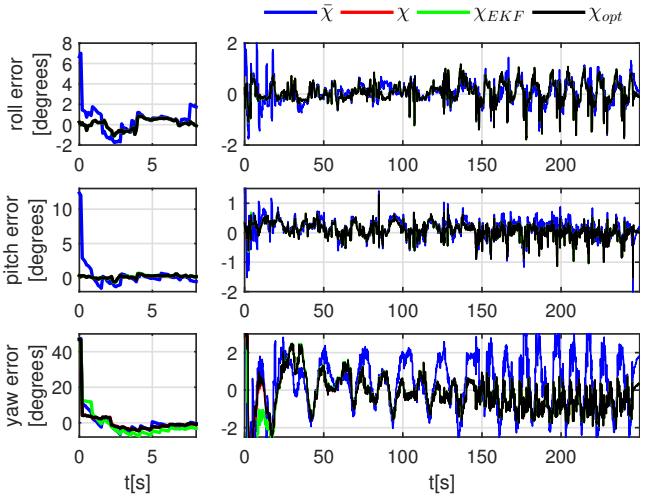

Fig. 10: Experiment A: Euler angle estimation errors. Two axis are chosen to show both transient and stationary behaviour

Experiment		A	B
RMSE[degrees]	$\bar{\chi}$	$[0.40, 0.31, 1.4]$	$[0.42, 0.77, 1.3]$
	χ	$[0.40, 0.25, 0.85]$	$[0.25, 0.58, 0.70]$
	χ_{EKF}	$[0.40, 0.25, 0.86]$	$[0.25, 0.58, 0.80]$
	χ_{opt}	$[0.40, 0.25, 0.85]$	$[0.25, 0.58, 0.68]$

TABLE III: RMSE for [roll angle, pitch angle, yaw angle] after convergence for all filters. Both experiment A and B.

when the yaw angle is changed rapidly. As discussed in Sec. II-D, these accelerations are not taken into account, as it is assumed gravity is the dominating acceleration measured.

B. Experiment B: Transit

In the second experiment the ROV is driving back and forth at different velocities. The ground truth position and Euler angles can be seen in Fig. 12. It is apparent that due to the difficulty in manual control of the ROV it is also turning, reaching yaw angles of up to around 0.9 radians. However, this also makes the experiment more varied, which can be

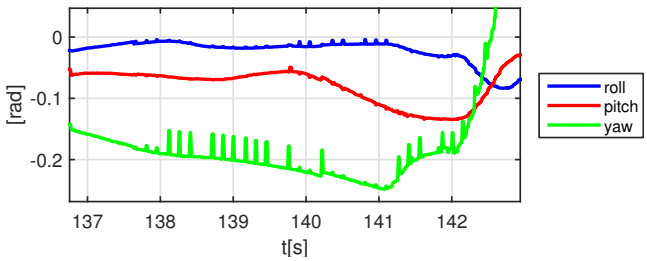

Fig. 11: Ground truth disturbance example. The spikes occuring for example around $t = 139\,\mathrm{s}$ does not seem to reflect realistic vehicle behaviour, and are therefore assumed to be disturbances

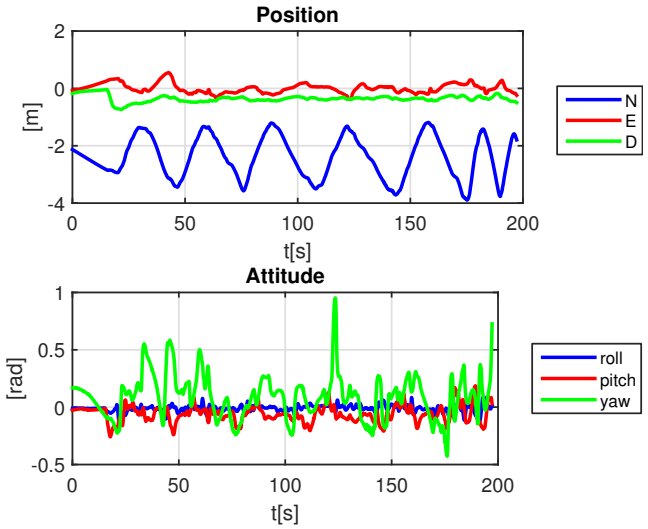

Fig. 12: Experiment B: Ground truth position and Euler angles from the Qualisys system

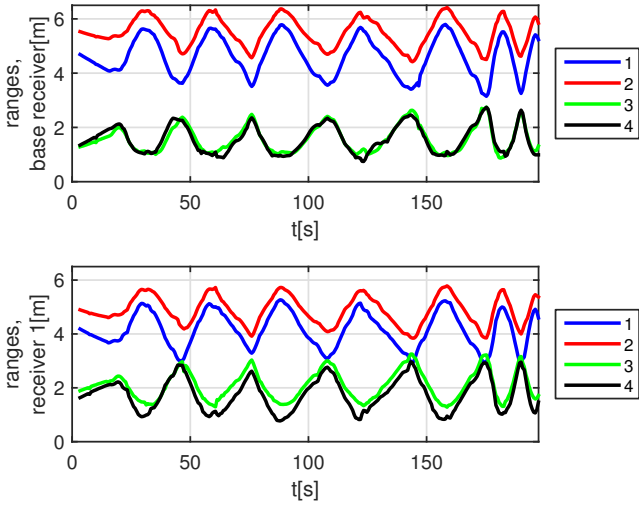

Fig. 13: Experiment B: Raw measured pseudo-ranges for both receivers. Pseudo-range i is the range measured from the sender at $\breve{\mathbf{p}}_i^n$.

seen as a good thing, as it seems the filter is also able to handle these cases. In addition it is also noteworthy that in experiment B the TDOA measurements start arriving at around 5 seconds into the experiment, as can be seen in the following figures, whereas in experiment A the measurements start arriving immediately.

The raw pseudo-ranges measured can be seen in Fig. 13. Throughout experiment B around $0.81\,\%$ of the pseudo-range measurements were rejected as outliers. The estimated and ground truth value of $\mathbf{d}_1^n$ is shown in Fig. 14, and the real and estimated position is shown in Fig. 15. The estimated rate sensor bias is shown in Fig. 16, and the Euler angle errors are shown in Fig. 17, with two different axis to show transient and stationary behaviour. As in experiment A, no error plot is shown for the estimated rate sensor bias, but at the end of the experiment the estimated rate sensor bias was $\mathbf{b}_{XKF} = \left[1.9 \cdot 10^{-4}, 4.9 \cdot 10^{-3}, -4.7 \cdot 10^{-3}\right]^T$ whereas in calibration this bias was found to be $\mathbf{b}_{cal} = \left[2.1 \cdot 10^{-4}, 5.0 \cdot 10^{-3}, -4.7 \cdot 10^{-3}\right]^T$, which is similar also for this experiment.

Also in experiment B the linearization point, $\bar{\chi}$, is less accurate than the output of the filter, χ, further supporting the claims made about the filter having both proven stability and close-to-optimal noise properties. Furthermore, in experiment B the EKF takes longer than the suggested filter to converge (around $18\,\mathrm{s}$ from the first TDOA measurement, compared to around $5\,\mathrm{s}$ for the suggested filter), whereas the suggested filter performs very similarly to the optimal filter throughout both experiments.

The results are similar to experiment A. The filter converges quickly, and stays close to the ground truth values. The RMSE after convergence for the different filters is shown in Tab. III. Also here the RMSE of the suggested filter is not much larger ($2.2\,\%$) than the error for the optimal filter. Note also that the

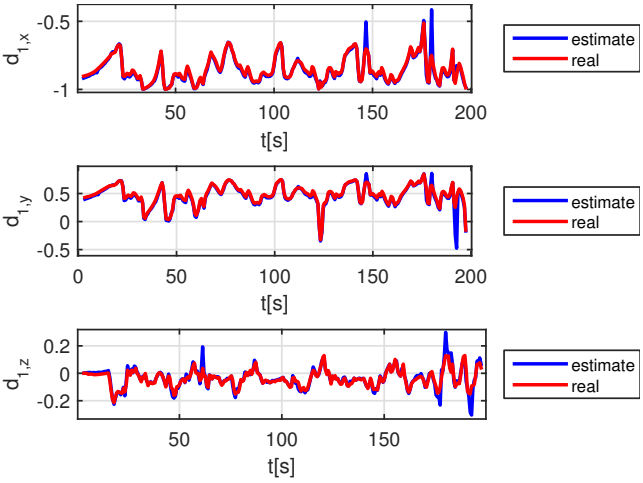

Fig. 14: Experiment B: Real and estimated values for $\mathbf{d}_1^n = [d_{1,x}, d_{1,y}, d_{1,z}]^T$

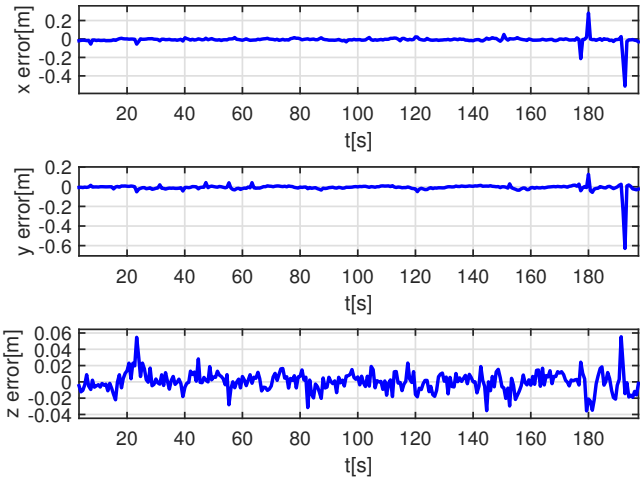

Fig. 15: Experiment B: Position estimation errors

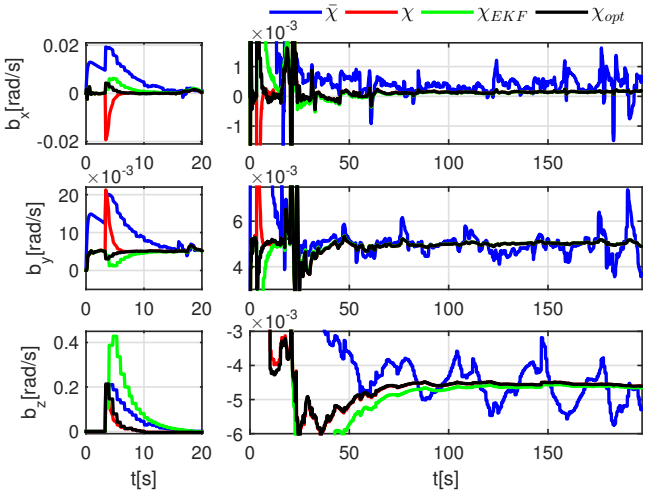

Fig. 16: Experiment B: Estimated rate sensor bias

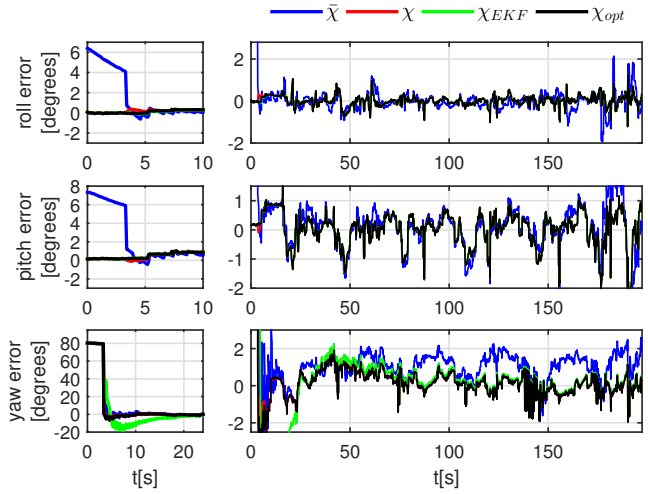

Fig. 17: Experiment B: Euler angle estimation errors. Two axis are chosen to show both transient and stationary behaviour

RMSE for yaw angle in the EKF is $15\,\%$ larger than for the suggested filter. However, also here the RMSE is most likely a combination of estimator and ground truth error, as the spikes in ground truth Euler angles are similar to the spikes in roll angle and pitch angle for experiment A, and seem to have the nature of disturbances rather than actual dynamic.

It can be seen in Fig. 17 that the pitch angle error increases slightly towards the end of the experiment, when the vehicle is moving faster, peaking at around $t = 192\,\mathrm{s}$. At around this time the vehicle is changing velocity from around $-0.4\,\mathrm{m/s}$ to around $0.4\,\mathrm{m/s}$ in slightly over one second, giving a larger acceleration than before. As in experiment A, these accelerations are not taken into account, as it is assumed gravity is the only acceleration measured.

VI. DISCUSSION

The performance of the applied filter is dependent on LBL sender- and receiver positions. The vectors from senders to the receiver should be as non-co-linear as possible. In the experiments performed in this paper the senders were placed in a trapezium-like shape in the NE-plane, and the ROV spent most of the time within the trapezium. Consequently, the geometry of the system was good for employing the suggested filter. However, situations where the vectors are very co-linear can happen either when the ROV is very far from the senders, or if the senders are placed almost co-linearly, neither of which is planned to be a scenario where the system is applied.

The performance of the filter is dependent on the tuning parameters for each subsystem. As the NLO in Σ_3 is based on a mathematical stability property, the tuning parameters have a more mathematical meaning, whereas Kalman Filters are based on the actual scenario and noise properties of the sensors provided. Therefore the tuning parameters in Σ_3 are chosen by trial and error, and other parameter values might give better results. However, in this paper it was also important to show that choosing the tuning parameters intuitively, based on a few simple principles was enough to get a well functioning filter.

As the performance of the EKF in the transient state is unpredictable, due to the inaccurate linearization point used in the filter, better performance wrt. transient error might have been achieved by tuning the EKF differently, especially by changing the $\mathbf{P}_0$-matrix to higher or lower values. However, tuning the EKF with the same intuitive tuning as the other filters gave a more fair comparison, as this tuning will cover all scenarios where the uncertainty in initial state described by $\mathbf{P}_0$ is accurate, whereas manipulation of $\mathbf{P}_0$ to an unrealistic value to get better results for a specific experiment will give more unpredictable behaviour in other scenarios.

The performance of the filter might be improved by compensating for the two acceleration measurement assumptions, that the accelerometer measurement has no bias, and that the vehicle acceleration is negligible compared to gravity. The validity of these assumptions is dependent on the accelerations of the ROV and the performance of the accelerometer bias calibration, along with the rate of change for the accelerometer bias. Ways of constructing filters with proven stability taking this into account for the given system are being considered, and is potential further work.

Low-pass filtering the IMU data before they are used as input to the filter is a common approach, and could also have been done in this paper. However, low-pass filtering results in a phase offset, which results in a delay in the IMU measurements. Furthermore, the filter seemed to give satisfactory results, as long as this noise was compensated for properly in the tuning of each subsystem.

As discussed in Sec. V-A, it seems that the ground truth data also contains some disturbances. Therefore, the RMSEs

calculated are not entirely accurate. However, they still function well as means of comparing the filters, as the ground truth noise is the same for all filters when calculating the RMSE. Furthermore, the ground truth noise seems to not occur often, and therefore does not have a significant effect on the calculated RMSE.

VII. CONCLUSIONS

Experimental validation of a filter for determining attitude and rate sensor bias based on TDOA and IMU measurements has been presented. The filter is based on the XKF principle, which is a cascade structure in which the output from a NLO is used as a linearization point for a LKF to achieve both proven stability properties and close-to-optimal performance wrt. bounded noise. In contrast to the EKF, which does not have proven stability, the filter has been proven to have local exponential stability, with singularities that are easily detectable, and not likely to occur for most conventional ROVs. Furthermore, the singularities can be handled by changing Euler angle representation.

Two experiments have been conducted, one in which the ROV is turning from side to side while stationary, and one where the ROV is driving back and forth. In both experiments the filter converges, and stays within a few degrees of the true state throughout the experiments. The RMSE of the suggested filter is equal to the non-implementable optimal filter in one experiment, and $2.2\,\%$ larger than the optimal filter for yaw angle in one experiment. Furthemore, the EKF takes longer than the suggested filter to converge, whereas the suggested filter estimates attitude very similarly to the non-implementable, optimal filter also in the transient state.

REFERENCES

[1] Bluerov2 webpage. http://www.bluerobotics.com/store/rov/bluerov2/. Accessed: 2017-07-01.

[2] Waterlinked webpage. https://waterlinked.com/. Accessed: 2017-07-01.

[3] Yaakov Bar-Shalom. *Tracking and data association*. Academic Press Professional, Inc., 1987.

[4] Pedro Batista, Carlos Silvestre, and Paulo Oliveira. Ges integrated lbl/usbl navigation system for underwater vehicles. In *2012 IEEE 51st IEEE Conference on Decision and Control (CDC)*, pages 6609–6614. IEEE, 2012.

[5] Pedro Batista, Carlos Silvestre, Paulo Oliveira, and Bruno Cardeira. Accelerometer calibration and dynamic bias and gravity estimation: Analysis, design, and experimental evaluation. *IEEE transactions on control systems technology*, 19(5):1128–1137, 2011.

[6] Clark E Cohen, Bradford W Parkinson, and B David McNally. Flight tests of attitude determination using gps compared against an inertial navigation unit. *Navigation*, 41(1):83–97, 1994.

[7] John L Crassidis, F Landis Markley, and Yang Cheng. Survey of nonlinear attitude estimation methods. *Journal of guidance, control, and dynamics*, 30(1):12–28, 2007.

[8] Jay Farrell. *Aided navigation: GPS with high rate sensors*. McGraw-Hill, Inc., 2008.

[9] Thor I Fossen. *Handbook of marine craft hydrodynamics and motion control*. John Wiley & Sons, 2011.

[10] Mohinder S Grewal, Lawrence R Weill, and Angus P Andrews. *Global positioning systems, inertial navigation, and integration*. John Wiley & Sons, 2007.

[11] Håvard Fjær Grip, Thor I Fossen, Tor A Johansen, and Ali Saberi. Attitude estimation using biased gyro and vector measurements with time-varying reference vectors. *IEEE Transactions on Automatic Control*, 57(5):1332–1338, 2012.

[12] Håvard Fjær Grip, Thor I Fossen, Tor A Johansen, and Ali Saberi. Globally exponentially stable attitude and gyro bias estimation with application to gnss/ins integration. *Automatica*, 51:158–166, 2015.

[13] Håvard Fjær Grip, Thor I Fossen, Tor A Johansen, and Ali Saberi. *Multisensor Attitude Estimation*, chapter 17, pages 291–314. CRC Press (Taylor & Francis Group),, 2016.

[14] Tarek Hamel and Robert Mahony. Attitude estimation on so [3] based on direct inertial measurements. In *Proceedings 2006 IEEE International Conference on Robotics and Automation, 2006. ICRA 2006.*, pages 2170–2175. IEEE, 2006.

[15] Jakob M Hansen, Thor I Fossen, and Tor Arne Johansen. Nonlinear observer design for gnss-aided inertial navigation systems with time-delayed gnss measurements. *Control Engineering Practice*, 60:39–50, 2017.

[16] Tor A Johansen and Thor I Fossen. Nonlinear filtering with exogenous kalman filter and double kalman filter. In *Control Conference (ECC), 2016 European*, pages 1722–1727. IEEE, 2016.

[17] Tor A Johansen and Thor I Fossen. The exogenous kalman filter (xkf). *International Journal of Control*, 90(2):161–167, 2017.

[18] Tor A Johansen, Jakob M Hansen, and Thor I Fossen. Nonlinear observer for tightly integrated inertial navigation aided by pseudo-range measurements. *Journal of Dynamic Systems, Measurement, and Control*, 139(1):011007, 2017.

[19] Erlend K Jørgensen, Tor A Johansen, and Ingrid Schjølberg. Enhanced hydroacoustic range robustness of three-stage position filter based on long baseline measurements with unknown wave speed. *IFAC-PapersOnLine*, 49(23):61–67, 2016.

[20] Erlend K Jørgensen and Ingrid Schjølberg. Attitude and gyro bias estimation using range-difference and imu measurements. In *Autonomous Underwater Vehicles (AUV), 2016 IEEE/OES*, pages 124–130. IEEE, 2016.

[21] Jack B Kuipers et al. *Quaternions and rotation sequences*, volume 66. Princeton university press Princeton, 1999.

[22] Richard B Langley et al. Dilution of precision. *GPS world*, 10(5):52–59, 1999.

[23] Angelo M Sabatini. Quaternion-based extended kalman filter for determining orientation by inertial and magnetic sensing. *IEEE Transactions on Biomedical Engineering*, 53(7):1346–1356, 2006.

[24] S Salcudean. A globally convergent angular velocity observer for rigid body motion. *IEEE transactions on Automatic Control*, 36(12):1493–1497, 1991.

[25] Malcolm David Shuster and S. D. Oh. Three-axis attitude determination from vector observations. *Journal of Guidance, Control, and Dynamics*, 2012.

[26] Bård B Stovner, Tor A Johansen, Thor I Fossen, and Ingrid Schjølberg. Three-stage filter for position and velocity estimation from long baseline measurements with unknown wave speed. In *American Control Conference (ACC), 2016*, pages 4532–4538. IEEE, 2016.

[27] Bjørnar Vik. Integrated satellite and inertial navigation systems. *Department of Engineering Cybernetics, NTNU*, 2009.

[28] Seong-hoon Peter Won and Farid Golnaraghi. A triaxial accelerometer calibration method using a mathematical model. *IEEE Transactions on Instrumentation and Measurement*, 59(8):2144–2153, 2010.